

**UCLA**

**UCLA Electronic Theses and Dissertations**

**Title**

Fabrication and Test of the Optomechanical Transducers

**Permalink**

<https://escholarship.org/uc/item/0s72h3sb>

**Author**

yerebakan, Talha

**Publication Date**

2021

Peer reviewed|Thesis/dissertation

UNIVERSITY OF CALIFORNIA

Los Angeles

Fabrication and Test of the Optomechanical Transducers

A thesis submitted in partial satisfaction  
of the requirements for the degree Master of Science  
in Electrical and Computer Engineering

by

Talha Yerebakan

2021

© Copyright by

Talha Yerebakan

2021

# ABSTRACT OF THE THESIS

Fabrication and Test of the Optomechanical Transducers

by

Talha Yerebakan

Master of Science in Electrical and Computer Engineering

University of California, Los Angeles, 2021

Professor Chee Wei Wong, Chair

In recent years, detectible noise spectral densities and displacement caused by optically driven optomechanical cavities have reached near the quantum backaction noise levels, if not at the same level. In addition to these improvements, using squeezed light as drive power has been proposed to increase the sensible noise spectral density beyond backaction, theoretically proving it is possible to go beyond the standard quantum limit (SQL) with quantum readout. Measurements at the thermodynamical bounds include slot-type photonic crystal cavities, which offer strong optomechanical transduction rates for optically pumped RF-readout force and field sense. On the other hand, fabrication and test of those devices introduce challenges.

In this thesis, a new three steps photolithography fabrication process is introduced. Although the current two-step fabrication process works well, it requires very high precision in alignment and etching timing. In this approach, we tried to solve those issues. As a result, we observed well-released devices and transmission loss as low as 24 dB in the preliminary results.

In addition to the new fabrication process, the thesis will introduce the testing and calibration of our optomechanical transducers. Testing the devices is a long and tedious process that involves the alignment of an optical driving source. Theoretical calculations such as mechanical quality factor and sensitivity agree with the data.

The thesis of Talha Yerebakan is approved

Benjamin S Williams

Sergio Carbajo Garcia

Kang Lung Wang

Chee Wei Wong, Committee Chair

University of California, Los Angeles

2021

## ACKNOWLEDGMENTS

I would like to thank my advisor Professor Chee Wei Wong, for his enduring mentorship throughout this research and for allowing me to pursue this unique study area. I would also like to thank my senior Ph.D. Student Jaime Flor Flores for his help and guidance with this project and for teaching me the essentials of nanofabrication, especially during the initial phase of my research. I would also like to thank him for the many stimulating intellectual discussions throughout my years of study. I would also like to express my gratitude to the various researchers. During the pandemic, they worked with me, especially Dr. Wenting Wang, Dr. James McMillan, Murat Can Sarihan, Dr. Andrei Matsko, and Dr. Vladimir Ilchenko, for various helpful inputs and suggestions.

Finally, I must express my heartfelt gratitude and respect for my family for providing me with support and continuous encouragement throughout my years of work and study. This accomplishment would not have been possible without them. Thank you.

## Contents

1 INTRODUCTION.....	1
Quantum Picture.....	3
Optomechanical Accelerometers .....	6
2 FABRICATION PROCESS.....	9
3-Step Fabrication Process .....	10
Full Nanofabrication Process .....	11
3 TEST RESULTS .....	14
Test Setup and Optical Transmission.....	15
Mechanical Oscillation and Acceleration Sensing .....	16
4 OTHER WORKS .....	21
Labview Spectrum Linearizer .....	21
5 FUTURE WORKS .....	23
6 CONCLUSION .....	25
7 REFERENCES.....	26

*List of Figures*

**Figure 1: Optomechanical Interaction.....1**

**Figure 2: Various Optomechanical Devices.....2**

**Figure 3: Optomechanical interaction simplified .....4**

**Figure 4: Accelerometer working principle. ....6**

**Figure 5: Optomechanical sensing unit.....7**

**Figure 6: Fabrication figures for an arbitrary accelerometer. ....10**

**Figure 7: SEM image of a halfway-fabricated accelerometer. ....12**

**Figure 8: Tools that used in fabrication and insertion loss quality factor relation.....13**

**Figure 9: Optical image of the photonic cristal from 2 different fabricated accelerometer. ....14**

**Figure 10: Experimental setup and transmission spectrum.. ....15**

**Figure 11: Mechanical oscillation. ....18**

**Figure 12: Narrow spectrum linearization program.....21**

**Figure 13: Novel mass design .....24**

# 1 INTRODUCTION

More than 500 years ago, Kepler figured out that light carries momentum by looking at the dust tails of the comets and seeing that they were moving away from the sun (1). Due to conservation of momentum, reflected light transfers some momentum on the reflection surface and creates radiation-pressure force.

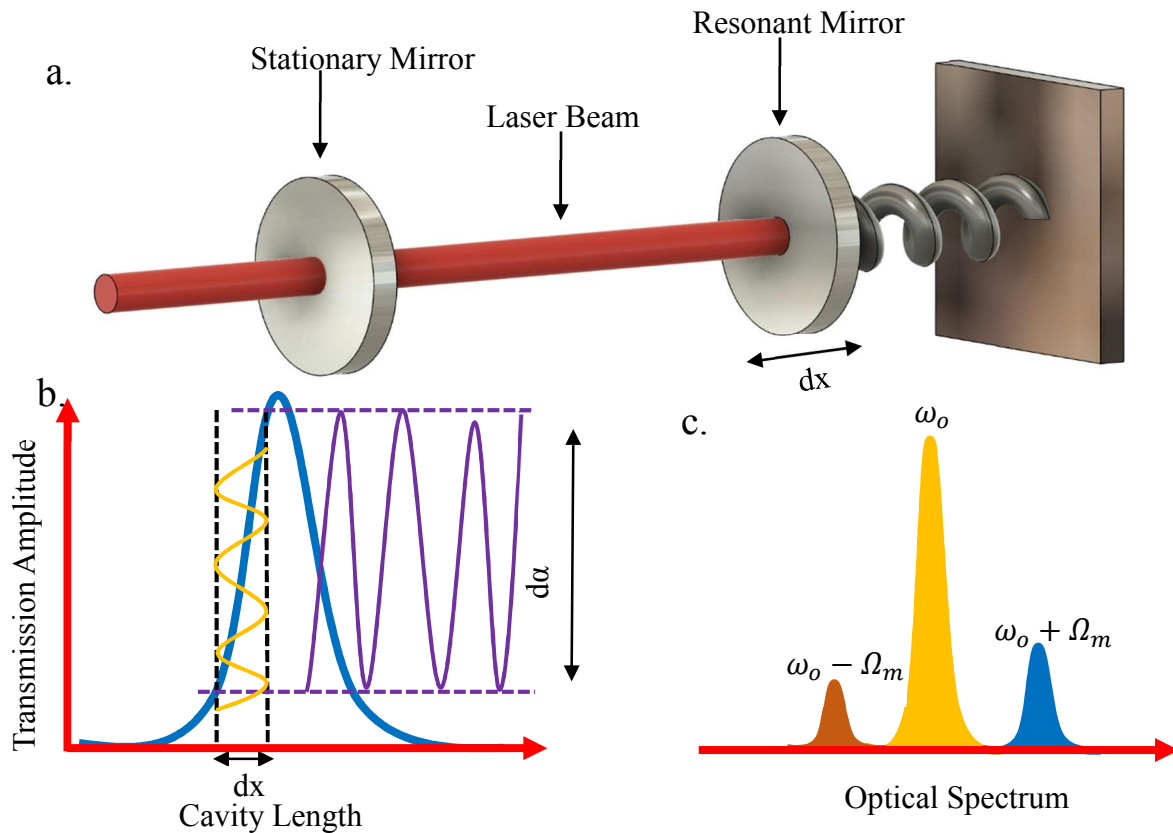


**Figure 1: Optomechanical Interaction.** a. Schematic of optomechanical interaction in an optical cavity. The optical cavity consists of a resonant (movable) mass and a stationary mass. Resonant mass behaves as mechanical oscillator. Transferred momentum from light to mass will move the resonant mirror at the resonant frequency of the mechanical oscillator. b. Changing cavity length shifts the transmission amplitude since the cavity length determines the optical mode frequency, and when it differs, the transmission amplitude also changes. This will create an amplitude modulation(2). c. Amplitude modulation at the mechanical resonant frequency can be understood as sideband around applied optical frequency(2).

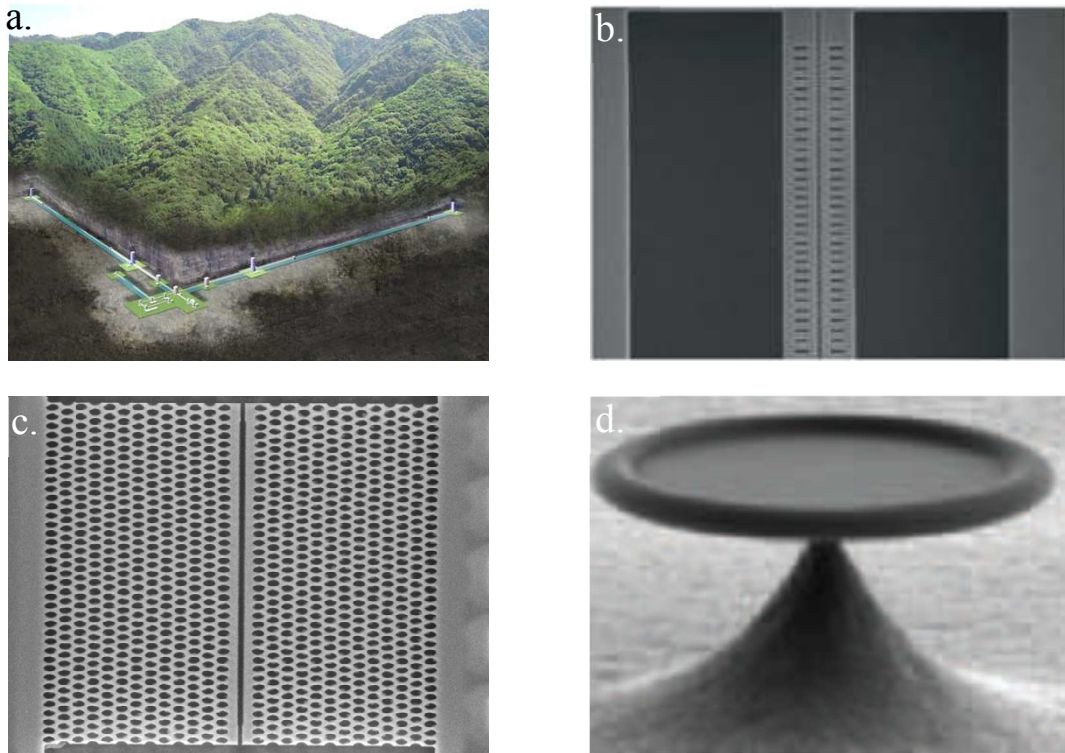


**Figure 2: Various Optomechanical Devices** a. Illustration of the KAGRA gravitational-wave detector, Gifu Prefecture, Japan. Image Credit: ICRR, University of Tokyo. b. Zipper cavity (3). c. Slot-cavity photonic crystal (4) d. High-Q silica micro-toroid cavity (5)

Figure 1a shows a schematic of how an optomechanical system works. Confined light inside the cavity gives momentum to the resonant mirror and moves it. Changing cavity length shifts the optical resonant frequency and introduces amplitude modulation in the transmission amplitude. Figure 1b demonstrates the transition from mechanical oscillation to amplitude modulation—the transmission amplitude changes as in Figure 1b with changing cavity length for a fixed optical frequency. Transmission amplitude has its peak value when the cavity mode and the optical frequency of the light are equal. Finally, Figure 1c shows that the modulation transforms into a sideband around the optical frequency. As seen in the same figure, the sidebands are not symmetric. The reason for this imbalance can be understood better in the quantum picture. Sidebands refer to either Stokes or Anti-Stokes lines, and one line is bigger than the other one depending on the working regime (2).

Real-life examples of different optomechanical cavities can be seen in Figure 2. Optomechanical cavities can be as large as LIGO or future gravitational-wave detector KAGRA in Japan (Figure 2a). On the other hand, they can be as small as nanocavities such as zipper cavity (3), slot-cavity photonic crystal (4), and micro-toroid cavity (5).

## Quantum Picture

Before going into the application, let us talk about the quantum picture of the optomechanics and discuss the working regimes.

In the quantum mechanical treatment, we can write the Hamiltonian of the mechanical harmonic oscillators as follows(6):

$$H = \hbar\Omega_m\hat{b}^+\hat{b} + \frac{1}{2}\hbar\Omega_m \quad (1)$$

Where  $\hbar$  reduced Planck constant,  $\Omega_m$  mechanical oscillation frequency, and  $\hat{b}^+$  and  $\hat{b}$  phonon creation and annihilation operator, respectively. And we can further introduce the position and momentum operators.

$$\hat{x} = x_{ZPF}(\hat{b} + \hat{b}^+) \quad (2)$$

$$\hat{p} = -im_{eff}\Omega_m x_{ZPF}(\hat{b} - \hat{b}^+) \quad (3)$$

Where

$$x_{ZPF} = \sqrt{\frac{\hbar}{2m_{eff}\Omega_m}}$$

(4)

is the zero point fluctuation (6). The same second quantization can be done for the optical field as well. Finally, when we write the total Hamiltonian of the system, we are going to have:

$$\hat{H}_{total} = \hat{H}_o + \hat{H}_{int}$$

(5)

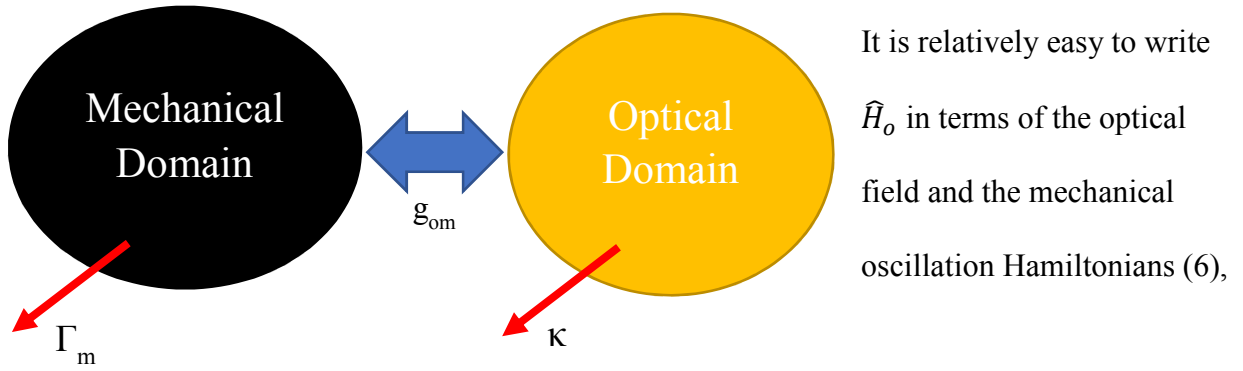


**Figure 3: Optomechanical interaction simplified**

$$\hat{H}_{total} = \hbar\Omega_m\hat{b}^+\hat{b} + \hbar\omega_{cav}(x)\hat{a}^+\hat{a}$$

(6)

For small perturbation the Equation 6 can be written as;

$$\hat{H}_{total} = \hbar\Omega_m\hat{b}^+\hat{b} + \hbar(\omega_{cav}(x=0) - g_{om}\hat{x})\hat{a}^+\hat{a}$$

(7)

$$\hat{H}_{total} = \hbar\Omega_m\hat{b}^+\hat{b} + \hbar\omega_{cav}(x=0)\hat{a}^+\hat{a} - \hbar g_{om}\hat{x}\hat{a}^+\hat{a}$$

(8)

$$\hat{H}_{int} = -\hbar g_{om} x_{zpf} \hat{a}^+ \hat{a} (\hat{b} + \hat{b}^+) \quad (9)$$

A unitary transformation of  $U = e^{i\omega_l \hat{a}^+ \hat{a} t}$  is applied to create a new interaction Hamiltonian (for more details, please see Ref. 6) where  $\omega_l$  is the laser frequency and defining  $\hat{a}$  in terms of an average value and fluctuation term, the interaction Hamiltonian term becomes;

$$\hat{H}_{int} = -\hbar g_{om} x_{zpf} (\bar{a} + \partial a)^+ (\bar{a} + \partial a) (\hat{b} + \hat{b}^+) \quad (10)$$

From Equation 10, the interaction Hamiltonian can be linearized (for more details, please see Ref. 6);

$$\hat{H}_{int}^{lin} = -\hbar g_{om} x_{zpf} \bar{a} (\partial a^+ + \partial a) (\hat{b} + \hat{b}^+) \quad (11)$$

The total Hamiltonian in the rotating frame can be written as;

$$\hat{H}_{total} = \hbar \Omega_m \hat{b}^+ \hat{b} - \hbar \Delta \partial a^+ \partial a + \hat{H}_{int}^{lin} \quad (12)$$

Where  $\Delta$  is the detuning of the laser with respect to cavity resonant frequency. This Hamiltonian creates 2 main working regimes for positive and negative detunings. For negative detuning ( $\Delta \approx -\Omega_m$ ), we can interpret that as one phonon is absorbed and intracavity energy increases, this regime is called cooling. On the other hand, for positive detuning ( $\Delta \approx \Omega_m$ ) intracavity energy decreases, and one phonon is created; this regime is called amplification. Thus, the amplitudes of the sidebands differ. For one sideband, the magnitude solely comes from the amplitude modulation, while for the other one the magnitude comes from both AM and cooling or amplification regimes (6).

## Optomechanical Accelerometers

With the introduction of small spacecraft such as CubeSats, reducing the size, power budget, and the price of navigation sensors such as accelerometers and gyroscopes became much more critical for reaching superior flight performance. Not long ago, cavity-optomechanical accelerometers were shown as compelling nominees for reducing size, power budget, and pricing and integration (7, 8).

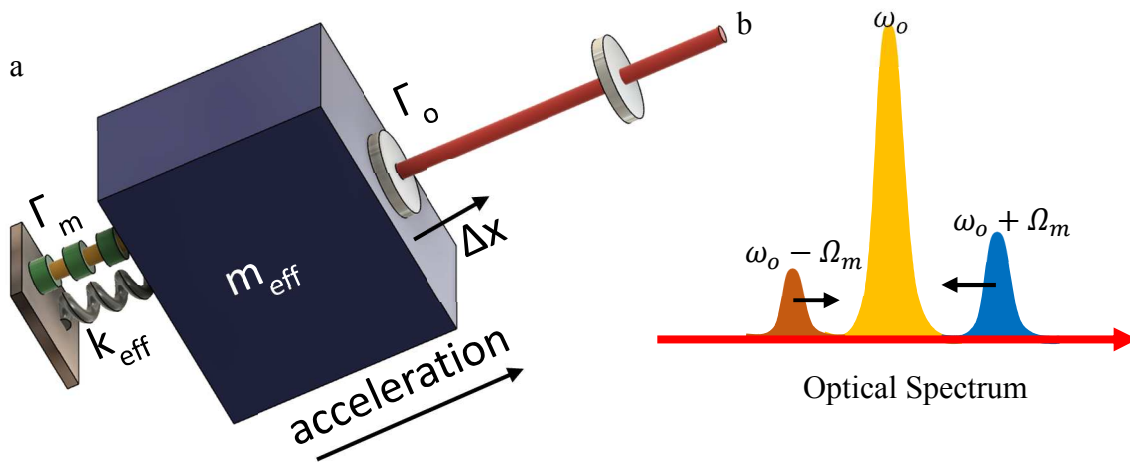


**Figure 4: Accelerometer working principle.** *a. Simple schematic of an optomechanical accelerometer. The free mirror is connected to the a sensing mass. Applied acceleration creates a force. This force moves the mass and changes the cavity length by  $\Delta x$ .  $k_{\text{eff}}$  is the effective spring constant and it affects the length change as well,  $F = m_{\text{eff}}a = \Delta x k_{\text{eff}}$ .  $\Gamma_m$  is the mechanical damping rate, and  $\Gamma_o$  is the optomechanically induced damping rate, and a note here, this damping rate can be negative, meaning that it gives the energy to the system. *b. Applied acceleration changes the cavity length and consequently mechanical frequency. By simple reading out the mechanical frequency change, we can measure the acceleration.**

In the paper published in 2012 by Oskar Painter and his group, a zipper cavity is used as an optical cavity. When an acceleration is applied to the mass, the separation between the zipper increases or decreases depending on the direction of the acceleration. Even though there is a change in the optical cavity resonant frequency, they lock the laser to the cavity. Therefore, their detuning is always the same. As discussed below, if there is no change in the detuning, there will be no shift at the RF frequency as well. Thus, it is impossible to measure the applied acceleration through mechanical frequency change with their method. However, they used the phase shift

method to measure the inertia, which caused the system to be bulky, expensive, and hard to integrate.

On the other hand, a new readout system and inertial sensor design described briefly in Figure 4 by Wong Group at UCLA promise easy integration, readout circuitry, and high resolution and stability.

The laser-driven optomechanical oscillation – and its laser readout – achieves the precision forces and fields sensing at the thermodynamical limits (8,9,10,11), enabling chip-scale inertial navigation and gravitational sensing. Figure 5c shows a scanning electron micrograph of the chip-scale cavity optomechanical inertial sensor, with a 7.2 nanogram

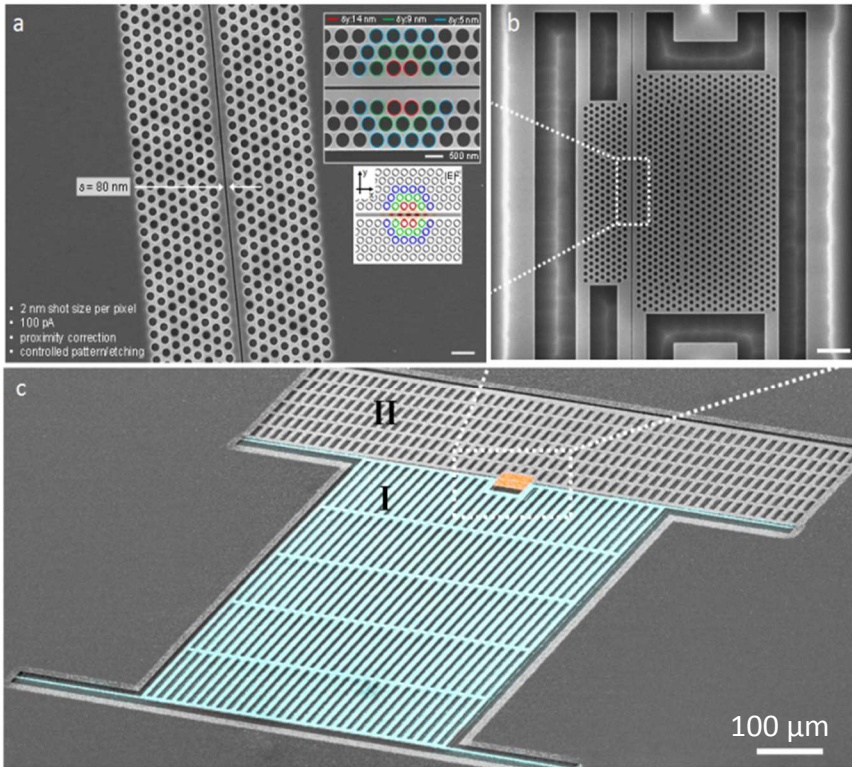


**Figure 5: Optomechanical sensing unit.** *a.* Zoom-in SEM picture of the photonic crystal cavity structure implemented in the released oscillator-mode RF-readout navigation unit. The photonic crystal devices demonstrated here are made by silicon. As shown in this figure, it has periodic hole array with a slot in the middle, which has width varying from 80 to 100 nm. This slot cavity inside the photonic crystal can form an engineered high- $Q$ , small-modal volume optical resonant cavity. The structure of this photonic crystal cavity is optimized using finite-difference time-domain (FDTD) simulation, and the optimized lattice perturbation, as shown in the upper inset, are 5-nm (blue); 9-nm (green); 14-nm (red). The simulation results, as shown in the bottom inset, shows that the electric field can be tightly confined in the optimized slot cavity, which can induce strong optical gradient forces, resulting in photon-RF transduction, one of the largest photon-RF transduction demonstrated. *c.* SEM of the accelerometer device(8)

motional mass  $m_{eff}$  (highlighted in blue; region I) and a stationary part (II) delineated. The central area (highlighted in orange; white dashed box) has an optomechanical photonic crystal

microcavity (8, 12), illustrated in the zoom-in micrograph of Figure 5b. Three segmented layers of photonic crystal holes are successively offset by 15-nm (blue), 10-nm (green), and 5-nm (red), respectively, forming a localized photonic crystal cavity with electromagnetic intensity  $|E|^2$  localized in an air-slot of 80-nm width  $s$  as shown in Figure 5b inset (4, 13, 14). This tight subwavelength  $|E|^2$  confinement gives rise to a strong optical gradient force (15, 16, 17), pushing against the sidewalls of the slot cavity with a radiation pressure-like force proportional to  $g_{om}|E_{cavity}|^2$ . Here  $g_{om}$  is the optical-to-motional displacement transduction coefficient (i.e., optomechanical coupling coefficient, in units of optical frequency shift GHz per nm displacement).  $E_{cavity}$  is the intracavity field envelope (8).

Because of the profoundly sub-wavelength confinement, resonant enhancement of the pump-laser optical gradient force in the slot-type optomechanical cavity that we have yields strong backaction. The optical and mechanical resonance frequencies of the cavity highly depend on the width  $s$  (please refer the Figure 1a for better understanding); in other words, resonant mass is connected to the free (resonant) mirror in Figure 1a. (8, 18 19). Acceleration moves the free mirror; for instance, if we apply an acceleration in the sensitive axis, the sidewall of the membrane of the slot cavity attached to mass will shift with displacement  $x_s$ , changing the slot width  $s$ . Thus, the mechanical resonant frequency  $\Omega'_m$  changes since the optomechanical stiffening shifts and it can be described by (8):

$$\Omega'_m = \sqrt{\Omega_m^2 + \left(\frac{2|\hat{a}|^2 g_{om}^2}{\Delta^2 \omega_c m_{eff}}\right) \Delta_o} = \sqrt{\Omega_m^2 + \left(\frac{2|\hat{a}|^2 g_{om}^2}{((\omega_l - \omega_c + g_{om} x_s)^2 + (\Gamma/2)^2) \omega_c m_{eff}}\right) (\omega_l - \omega_c + g_{om} x_s)} \quad (13)$$

where  $\Delta$  is the detuning of the laser (difference between the cavity resonance frequency and the applied laser frequency),  $\Omega'_m$  and  $\Omega_m$  are the changed and original mechanical frequencies,

respectively,  $|\hat{a}|^2$  is the total photon energy inside the cavity,  $g_{om}$  is the optomechanical coupling rate,  $m_{eff}$  is the effective mass,  $\Gamma$  is the optical cavity decay rate and  $\omega_e$  is the optical resonance frequency. For small perturbations, shift in the mechanical resonant frequency ( $\Omega'_m - \Omega_m$ )

Our driven coherent oscillation mode has a narrow RF linewidth at the sub-Hz level, subsequently high mechanical quality factor. The coherent drive is enabled by the significant  $g_{om}$  transduction in our enhanced slot-type cavity (with  $g_{om}$  at 37.1 GHz/nm (8), but in our current device we calculated it to be around 25 GHz/nm). In our previous work, the sensing mass has enabled our acceleration measurements with a resolution of  $8.2 \mu\text{g}/\text{Hz}^{1/2}$ , without any laser locking system to achieve stable laser. In addition, our group previously have demonstrated a thermal-noise-limited sensitivity for the accelerometer of 2.62 mg per Hz of RF shift in pre-oscillation mode and 625  $\mu\text{g}$  per Hz in oscillation mode (8). There is a feedback control loop in charge of the laser stabilization and the frequency matching, which will be discussed later.

## 2 FABRICATION PROCESS

The optomechanical accelerometer's fabrication process consists of 2-step of photolithography and wet Buffered Oxide Etcher (BOE) etching. In the first lithography and etching step, the aim is to fully etch the oxide layer on top of the device, as seen in Figure 6.

The full release of the resonant mass is achieved by the second lithography and etching steps.

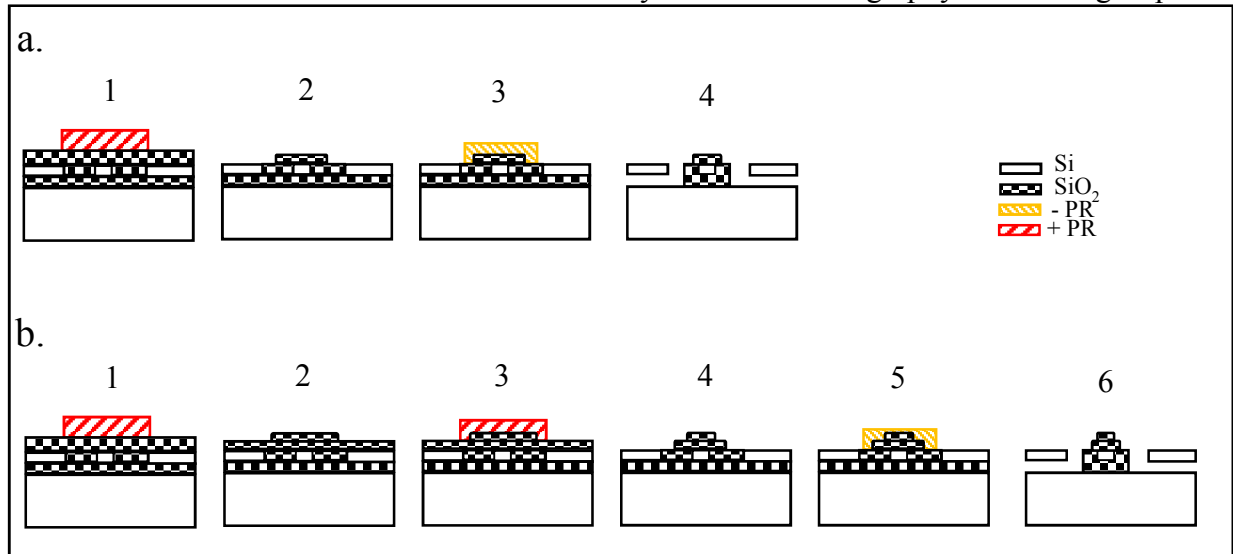


**Figure 6: Fabrication figures for an arbitrary accelerometer.** a. Step-by-step previous nanofabrication process. 1 and 3 show the diagram of the device after each photolithography step. 2 and 4 show the diagram of the chip after each etching. b. 1, 3 and 5 show the diagram of the device after each photolithography step. While 2, 4, and 6 show the chip after wet etching.

Even though this process works perfectly fine, the alignment and the etching time are crucial.

Half a micrometer misalignment or a couple of seconds over or under etching can cause the device to malfunction. Thus, we introduced another fabrication process inspired by the first process. The issue we frequently encountered was the cladding on the waveguide fully etched, and the waveguide was exposed. As a result of this etching, the insertion loss to photonic crystal increases by a factor of 4 (from 30 dB to 24 dB).

To solve the issue, we replaced the first photolithography with 2-step lithography and wet etching. This approach reduced the undercutting, the main reason for the problem, and allowed us to keep the insertion loss as low as possible.

### 3-Step Fabrication Process

A detailed explanation of our newly introduced fabrication process consisting of three recurring lithography's and BOE etching steps can be seen in Figure 6b. This new introduction aims to fully release the stationary and resonant masses while keeping the top silica layer of the waveguide—positive lithography and wet etching to reduce the silica thickness on the masses is applied during the first 2-steps namely Steps 1 and 2. However, if those 2 steps were to be combined and create a single step, the waveguide would be exposed to air because of the undercutting. Therefore, adding one more lithography step and reducing the first etching time covers the undercut region and successfully preserves the top oxide. Finally, a negative photoresist, nLoF 2020, in the final lithography process is used. The reason is some sections of the mass have been undercut, which would cause resistance development issues.

### **Full Nanofabrication Process**

The chips were prefabricated at a facility in Singapore. First, the IME does E-beam lithography and patterning. Then, they sent us the photoresists covered the wafer to protect it. After this point, the final fabrication process starts. Finally, we release the devices in Nanolab and CNSI cleanroom.

The first photolithography is done with a positive photoresist called AZ 4620. We use this photoresist since it is thicker than other positive photoresists in the Nanolab, providing us mass transport limited etching and thus better process control. 8-micrometer thick photoresist has covered the chip. Next, we align the chip with the Karl Suss Aligner in the Nanolab. After the development process with AZ 400K developer, the chip is etched with BOE for 5 minutes. And, this etching finalizes the first lithography and etching step.

The second photolithography and etching step are not different than the first one. We have this step because we can cover the undercut region for the subsequent etching; please see Figure 7b step 3. However, there is a slight change in the etching time. We increased the time by 3 minutes, and there are 8 minutes of etching in total. The amount of time is enough for us to reach the silicon layer on the masses.

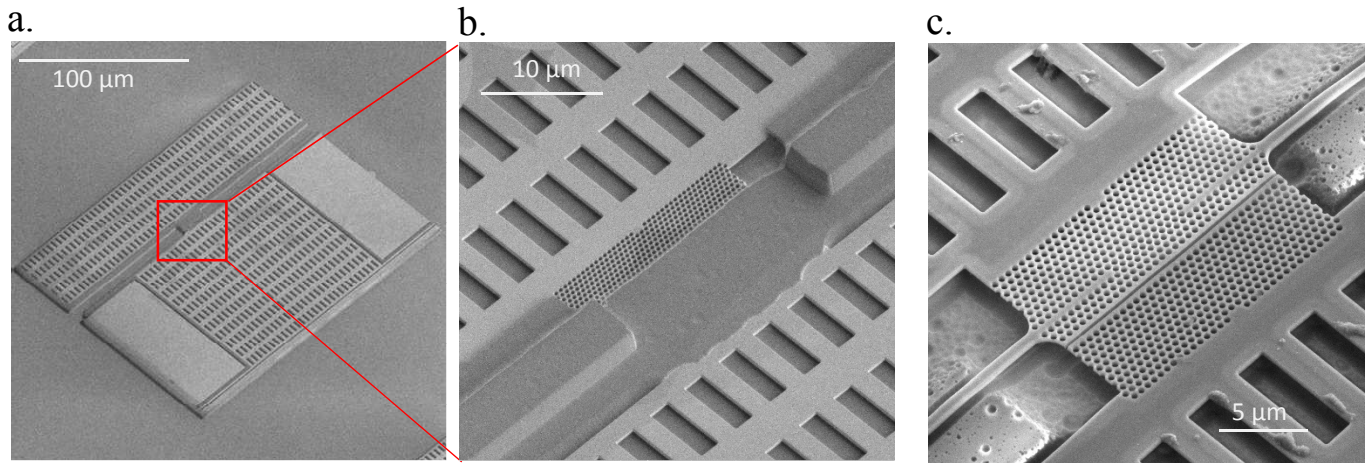


**Figure 7: SEM image of a half-fabricated (namely at state 4 in Figure 6b) accelerometer.** *a. A SEM image of an accelerometer. The slot-type photonic crystal where the optical cavity is located in the middle of the crystal showed by a red square. b. SEM image of the half-buried crystal and fully buried waveguide by the SiO<sub>2</sub>. Preserving the top oxide layer at the cladding of the waveguide decreases the insertion loss by a factor of 4. c. An air-bridged photonic crystal, however, the waveguide exposed to the air increasing the insertion loss.*

Finally, we use a negative photoresist in the third photolithography, namely nLoF 2020. The thickness of the resist in this step is not too important; therefore, we use a relatively thinner photoresist with a thickness of 2 micrometers. After aligning with the Karl Suss aligner in the Nanolab, we develop the photoresist with AZ 300 MIF developer for one minute. At this point, we get ready for the final etching. We do the Descum at Nanolab and the final etching for 27 minutes at the CNSI clean room. A side note here, Descum is a very crucial step in the fabrication since, after development, not every photoresist on the etching window washed away; there is still a thin layer of photoresist that stays with a thickness of a couple of tens of nanometers. Thus, we cannot see that under the optical microscope; however, it will cause some

etching issues. Therefore, a delicate plasma etching is applied to the chip before final etching to prevent this problem.



**Figure 8: Tools that used in fabrication and insertion loss quality factor relation.** a. Karl Suss mask aligner. In order to successfully complete the lithography, we use the manual mask aligner at the nanolab. AZ 4620 Positive photoresist is exposed for 90 seconds with 8 mW UV light, and the nLoF 2020 is exposed the light for 10 second with the same power. b. A Tousimis Autosamdri-815 Critical Point Dryer (CPD). CPDs are crucial to take the SEM images of bio-samples, however, it is also frequently used in MEMs device fabrication after wet etching process, dry etch and vapor etche do not require any post processing with the CPD. However, since dry etche can only do anisotropic etching, releasing the devices with dry etch only is not an option, and for the vapor etche, the etcher should work at higher temperatures, the process buckles the devices. Thus, we decided to use wet etching and CPD, even though it is a little bit more tedious. c. Mechanical quality factor vs input power and insertion loss plot.

Even though the wet etching allows us to undercut at room temperature, unlike the vapor HF etching, a post-process of drying is needed. Before that, we clean the chip overnight using an AZ 880 Stripper. Then, the cleaned chip is transferred to the Tousimis Autosamdri-810 Critical Point Dryer in the CNSI. The significance of the critical point drying is that the devices do not collapse because of the surface tension of the liquid under the released devices.

In Figure 8, the tools used in the fabrication process and the mechanical quality factor insertion loss relation can be seen. Figure 8a shows the same Karl Suss mask aligner model in the Nanolab to fabricate the device. Similarly, a newer model of the Tousimis critical point dryer is illustrated in Figure 8b. Figure 8c, on the other hand, reveals insertion loss-input power and

mechanical quality factor relation. It is clear that reducing insertion loss increases the mechanical quality factor for the same input power. However, the crucial part is that the mechanical quality factor does not change significantly for the higher loss. Therefore, even if the corresponding device has a sizeable optomechanical coupling coefficient, we cannot achieve high performance from this device. Most of the time, those transducers do not work at all. The plot in Figure 8c shows and explains why we have changed our previously well-established fabrication process, and the derivation for Figure 8c will be discussed in the following chapter.

### 3 TEST RESULTS

Each fabricated chip contains over 100 devices; testing all 100 devices is tedious work. Therefore, we check the devices under an optical microscope and see whether everything is alright. For instance, we do not test the accelerometers without a coupler or waveguide or if the

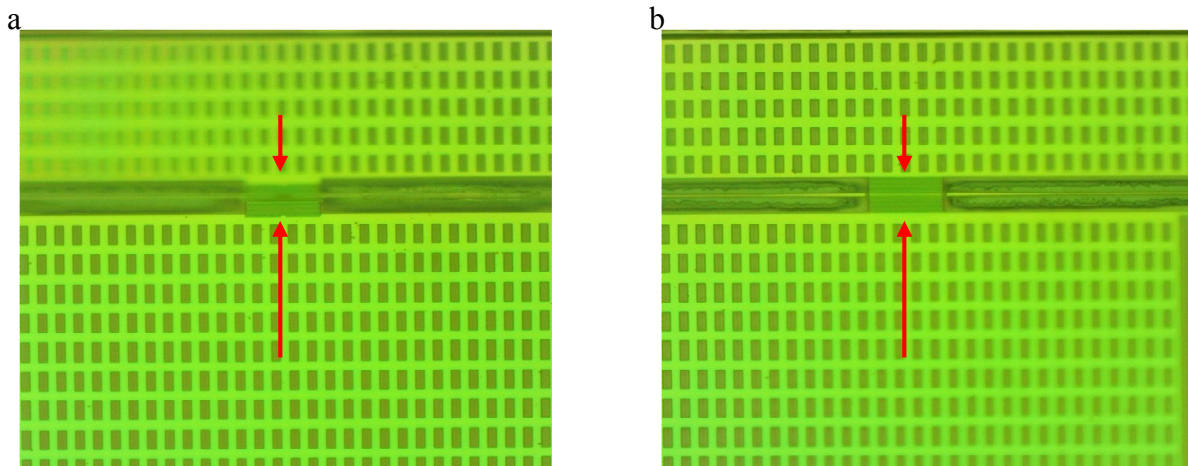


**Figure 9:** *Optical image of the photonic crystal from 2 different fabricated accelerometer. a. The halves of the crystal are not well-aligned. b. Optical image of a well-aligned crystal from a released device.*

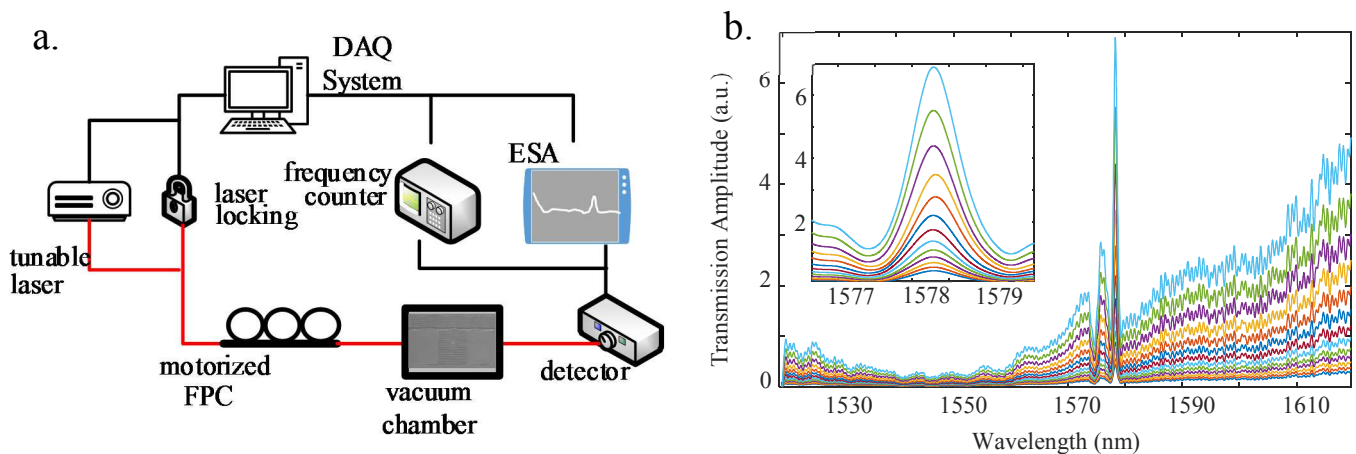
photonic crystal is not well-aligned. The alignment of the photonic crystal is critical and must be checked under the optical microscope since it is impossible to see the alignment with naked eyes.

Figure 9 shows the optical image of 2 different fabricated devices. In Figure 9a, a height difference between the halves of the photonic crystal occurs after the air bridge and release. Thus, the corresponding photonic crystal will not have a high optical quality factor, and the optical quality factor is essential to achieve a powerful optomechanical interaction. On the other hand, the photonic crystal in Figure 9b is well-aligned. Therefore, these kinds of devices are selected as worth testing. However, there is no guarantee that those devices will work.

### Test Setup and Optical Transmission

Figure 10a illustrates the experimental setup. First, an optomechanical transducer vacuum environment is coupled to the Santec 510 tunable laser. Next, we used the DAQ system and the Labview code written by Jaime Flor Flores to capture the plot in Figure 10b. Next, Santec 510 laser is swept from 1520 nm to 1620 nm, storing output data. Once we find a decent optical quality factor, we check for the mechanical mode using a Keysight Technologies N9010A Electrical Spectrum Analyser (ESA).

Further characterizations and measurements are done after we lock the laser to our stable



**Figure 10: Experimental setup and transmission spectrum.** a. Experimental setup. b. Optical transmission spectrum of the photonic crystal for different input powers. Inset shows the optical mode.

Menlo comb system. Then, a Labview code reads the modulated output through an optical

detector connected to a frequency counter and the ESA. Finally, the measured data is stored by the same Labview code on a computer.

The optical transmission spectrum can be seen in Figure 10b. 2 optical modes exist at 1572 nm and 1579 nm with slightly low optical quality factors of  $\sim 800$  and  $\sim 2000$ , respectively. Probed by lensed fibers from sides of the optomechanical cavity, Figure 10b shows the measured optical transmission spectrum under different input powers (from lowest to the highest, -7, -6, -5, -4, -3, -2, -1, 0, 1, 2, 3, 4, 5, 6, 7 dBm inputs). For example, under a slightly high-input power (5 dBm), the loaded cavity quality factor  $Q_o$  is measured at  $\approx 2000$  (intrinsic cavity quality factor  $Q_{in}$  was reported as  $\approx 13200$  for the same crystal(8)). And in the inset of this figure, we can see a very slight red-shift in the optical mode with increasing driving power. However, for more red-shift, we need a higher optical quality factor.

## **Mechanical Oscillation and Acceleration Sensing**

Figure 11a shows the power spectral density of the mechanical oscillation domain and the different and higher mechanical modes. The fundamental mode and its double folded degenerate mode can be distinguished clearly since they have the largest SNR in between the other modes. The mechanical oscillation at the frequency of 83 kHz is not an orthogonal mode but rather the second harmonics of the fundamental mode. Also, it is possible to see the sidebands as well separated from each other by 2 kHz. Additionally, the other orthogonal modes are also seen in the spectrum at 45, 53, and 125 kHz frequencies. And the shapes of the orthogonal modes are different than the fundamental mode shape illustrated in the inset with the help of FEM simulation (COMSOL). Figure 11b shows the 2D map of the mechanical mode around 42 kHz.

Fundamental mode and the double-folded degenerate mode can be seen in this plot. The reason why there is such behavior is explained above; please see the Equation 13.

$$\Omega'_m = \sqrt{\Omega_m^2 + \left( \frac{2|\hat{a}|^2 g_{om}^2}{((\omega_l - \omega_c + g_{om}x_s)^2 + (\Gamma/2)^2)\omega_c m_{eff}} \right) (\omega_l - \omega_c + g_{om}x_s)} \quad (14)$$

When there is constant acceleration  $g_{om}x_s$  term is constant. By changing the laser frequency  $\omega_l$ , we can shift the mechanical resonant frequency, and this equation is experimentally proven in the 2D map in Figure 11b.

Figure 11c demonstrates the theoretical and experimental results for the mechanical quality factor versus applied laser power in terms of dBm. As seen in the figure, after 0 dBm, the mechanical quality factor increases exponentially. The point where we have a sudden jump is called the threshold power for the oscillation mode. Even though there is no exact definition for the threshold power, and thus it is impossible to choose a precise point for this value, it is feasible to make an appropriate approximation. We estimated the threshold power to be around 0 dBm for the current working accelerometer. Inset shows the mechanical mode and the Lorentzian fit for the corresponding mode. The mechanical quality factor is calculated to be around 10000 for this particular data.

The mechanical quality factor, which is related to the damping coefficient, can be found from the total mechanical loss formula;

$$\Gamma_{eff} = \Gamma_o + \Gamma_m \quad (15)$$

Where  $\Gamma_m$  is the intrinsic mechanical loss rate, and  $\Gamma_o$  is the damping rate induced by the optomechanical interaction, and is shown in the following equation (4,20):

$$\Gamma_o = -\frac{\omega_o}{2\Omega_m L_{om}^2 m_{eff}} \left( \frac{2\kappa_{ex}}{\kappa^2 + 4\Delta^2} \right) \left[ \frac{\frac{\kappa}{2}}{(\Delta - \Omega_m)^2 + \left(\frac{\kappa}{2}\right)^2} - \frac{\frac{\kappa}{2}}{(\Delta + \Omega_m)^2 + \left(\frac{\kappa}{2}\right)^2} \right] P$$

(16)

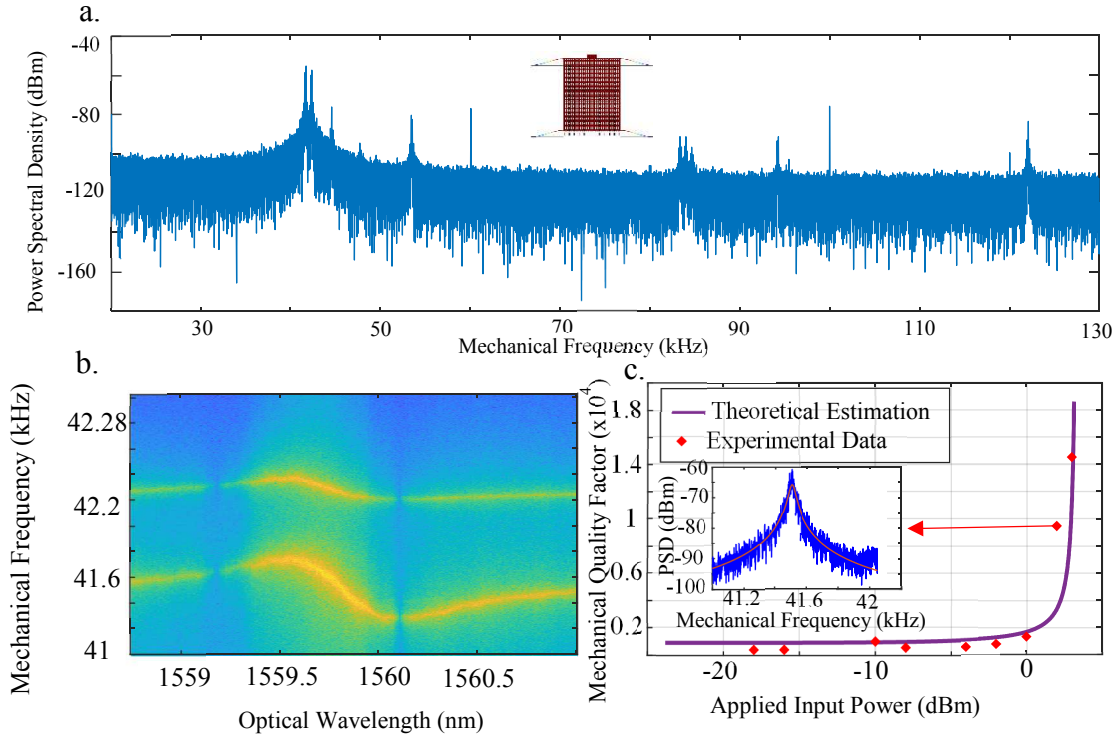


**Figure 11: Mechanical oscillation** a. Measured laser Power Spectral Density (PSD) from ESA of the optomechanical accelerometer (OMA). The fundamental mode resonance frequency is at  $\approx 41.5$  kHz. Measurement has been done at 10 Hz resolution bandwidth from 1 kHz to 130 kHz. Top middle inset is the FEM simulation of the fundamental mode. The second peak at 42 kHz arises because of the double-folded degeneracy. The resonance Lorentzian has a mechanical quality factor ( $Q_m$ ) of  $\approx 10000$ . It is also possible to see second harmonic of the fundamental mode around 83 kHz with the sidebands. The peaks at the 45 kHz, 53 kHz, 125 kHz are the other orthogonal modes that the mechanical system has. On the other hand, the rest of the peaks are detector noise. b. Mechanical resonant frequency  $\Omega_m$  vs. detuning  $\Delta$  map of the optomechanical accelerometer. The applied laser power is at 2 dBm. It is easy to see the optomechanical stiffening and softening. The fundamental mode has frequency change of almost 600 Hz, while the double-folded degenerate mode has only 100 Hz. c. Mechanical quality factor versus input power plot. As seen in the figure, the quality factor increases exponentially. The point where exponential behavior starts is called the threshold power for the oscillation mode. The red points on the graph are the mechanical quality factor at the corresponding input powers. Finally, the inset shows the measured and Lorentzian fitted mechanical mode for the 2 dBm input power.

Where  $\omega_o$  optical frequency,  $\Omega_m$  mechanical oscillation frequency,  $L_{om}$  mode length,  $m_{eff}$  effective mass,  $\Delta$  detuning,  $P$  is the intracavity and  $\kappa_{ex}, \kappa$  the external and total cavity decay rates, respectively. Laser frequency and mechanical frequencies are already known. Effective mass,  $m_{eff}$  is calculated simply by multiplying the mass volume and the density of the silicon and found to be 7.2 nanograms, as indicated above. For the  $\kappa$  values;

$$\kappa = \kappa_{in} + \kappa_{ex} \quad (17)$$

Where  $\kappa_{in}$  the intrinsic cavity decay rate and equal to;

$$\kappa_{in} = \frac{\omega_c}{Q_{in}} \quad (18)$$

The intrinsic optical quality factor  $Q_{in}$  is reported as 13000 for the same type of crystal (4). From these values and equations, cavity decay rates are estimated. The challenging part, on the other hand, was to determine the effective mode length  $L_{om}$ . The given equation is (4)

$$L_{om} = \frac{\omega_c}{g_{om}} \quad (19)$$

Where  $g_{om}$  is the optomechanical coupling rate.  $g_{om}$  can be described as the change in the optical cavity resonance per the change in the slot width  $s$ , or:

$$g_{om} = \frac{d\omega_c}{ds} \quad (20)$$

Even though there are different approaches to (21, 22) determine optomechanical coupling rate, we came up with another practical solution. We know that the coupling rate is constant for small perturbations on the slot width; this is the reason why there is a linear mechanical frequency change for applied acceleration. Consequently, we take the optical transmission spectrum when applying different accelerations inside the linear regime. From applied acceleration, we can find the change in the slot width  $s$ . We determine the cavity resonance frequencies from the optical transmission spectrum and obtain a plot where the x-axis is the slot width change. The y-axis is the cavity resonance frequency change. The slope gives us the optomechanical coupling rate around 25 GHz/nm. However, there is another term we should find, which is mechanical damping rate,  $\Gamma_m$ . As seen from the equation,

$$\lim_{P \rightarrow 0} \Gamma_o = 0 \tag{21}$$

$$\lim_{P \rightarrow 0} \Gamma_{eff} = \Gamma_m + \lim_{P \rightarrow 0} \Gamma_o = \Gamma_m = \frac{\Omega_m}{Q_m} \tag{22}$$

we can obtain the mechanical damping rate value by simply measuring the mechanical quality factor of the fundamental mode in different input power and gradually decreasing it and taking the limit.

After finally finding the mechanical damping rate and the damping rate induced by the optomechanical interaction in terms of the power only, we can find the effective damping rate;

$$\Gamma_{eff} = \Gamma_o + \Gamma_m = \frac{\Omega_m}{Q_m} \tag{23}$$

## 4 OTHER WORKS

In this section, some other relatively small research activities will be discussed.

### Labview Spectrum Linearizer

During the research time, we also have developed an automated procedure for the accurate acquisition of the optical transmission spectrum of an optical cavity. The process involves Labview codes and is suitable for various measurement systems. However, the main objective is to use the program for an optomechanical-based accelerometer. As indicated before, optomechanical accelerometers promise superior performance in terms of bandwidth and resolution. First, however, they have to be characterized.

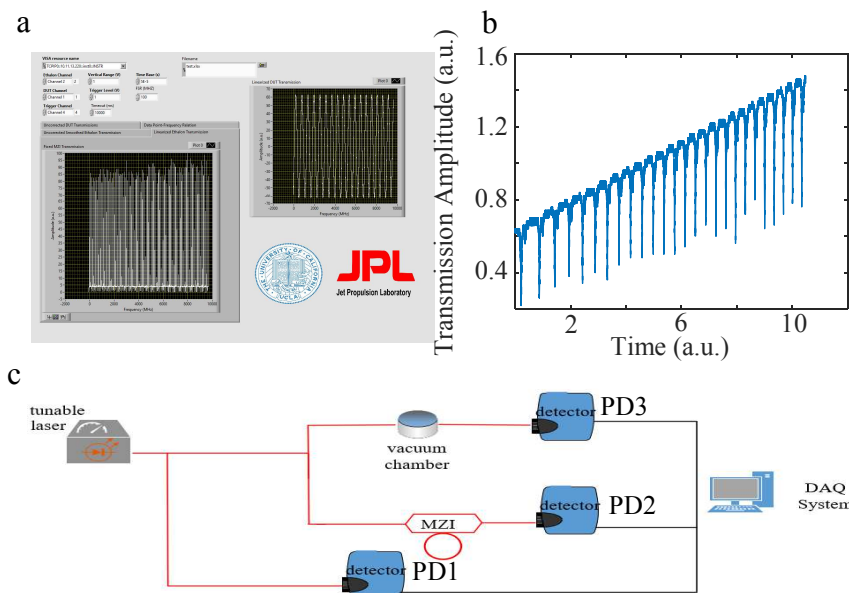


**Figure 12: Narrow spectrum linearization program a. Labview program. b. Laser sweep non-linearity. c. Setup**

As indicated above, our accelerometer design also has an optical cavity attached to the sensing mass, and one should characterize the optical cavity for modeling and

measurements. A model should be created by using a tunable laser. However, the nonlinearity between tuned current and generated wavelength of the laser creates an obstacle to detailed characterization of the sensor, such as the optical quality factor. The objective of this study is to linearize this relation in real-time by using the Labview program.

Figure 12b shows the transmission spectrum of the reference cavity. Each dip in the graph represents the cavity mode and should be separated by a known Free Spectral Range (FSR). However, it is clear that the separation between the modes is not the same in time. The reason behind it is the nonlinearity between applied current and laser frequency. The study aims to fix nonlinearity by creating a graph where the x-axis is the frequency, and the y-axis is the amplitude. The program will allow us to characterize the driving optical cavity accurately.

The experimental setup for the device characterization can be seen in Figure 12c. Again, a tunable laser (Velocity Laser at JPL and Santec 510 Laser at UCLA) is responsible for characterization. The laser is connected to a 90:10 beam splitter (BS), 10 percent goes to photodetector 1 (PD1), and records the laser intensity with respect to sweep time. The rest of the power goes to another BS with the same ratio. While most of the power goes to Device Under Test (DUT), 10 percent goes to reference interferometer. Transmissions of MZI and DUT are monitored through PD2 and PD3, respectively. All photodetectors are connected to a computer with a DAQ system; further data processing and fixation are done through a computer program.

The compensation algorithm consists of a couple of steps. Initially, the intensity change due to the current sweep is zeroed. This step is called baseline correction. Next, a linear line is fitted to the Mach-Zender Interferometer transmission spectrum and subtracted from the baseline correction step. However, due to the dips in the transmission spectrum, the baseline correction still does not give us a straight line; rectification is still needed to change from dips to peaks. For

rectifying, the subtracted spectrum is multiplied by a negative number (-150, but it does not matter). Finally, a lower limit is set to rectify and straighten the transmission spectrum entirely using a built-in function. After this step, the peaks on the range should be located. At this point, another problem occurs. Due to high-frequency noise in the data, there is more than one peak location in each peak. Thus, the built-in peak detection algorithm detects multiple peaks where it should detect only one. The simplest solution to this issue is to use the built-in low-pass filter. Labview 2020 has a built-in low-pass filter; however, the user should determine the cutoff frequency. The program has had this property since different reference interferometers and measurement equipment might have distinctive noises. Each location of peaks shows the data number where the peaks are.

Additionally, the frequency of each peak is also known since the Free Spectral Range (FSR) of the reference interferometer is given by the user. Using this information and data interpolation makes assigning a frequency value for each data number possible. Therefore, one can quickly transform data numbers into frequency values and replace the new frequency array as the new X-axis in the graph.

## **5 FUTURE WORKS**

While we achieved an insertion loss of 24 dB, the buckling on chips remains a challenge. Because of the buckling, we cannot obtain optical cavity mode, or the optical quality factor is so small that we cannot generate mechanical mode. Furthermore, it has been already shown that the buckling depends on the beam length. Thus, having a smaller mass attached to the crystal will help to reduce the buckling. However, on the other hand, reducing the mass will increase the thermal noise (3). To bypass this problem, we have developed a novel mass design.

Figure 13a shows the newly designed mass structure. As seen in the figure, the crystal is held by a pair of thin beams. Since the beams are much narrower than the original beams holding the central mass below, the original beams will dominate the spring constant. Thus, we can resolve the buckling issue without increasing the spring constant. However, we still need to optimize the mass design using COMSOL and fabricate it. Additionally, we are still optimizing the 3-step fabrication process, changing the etching times and the mask.

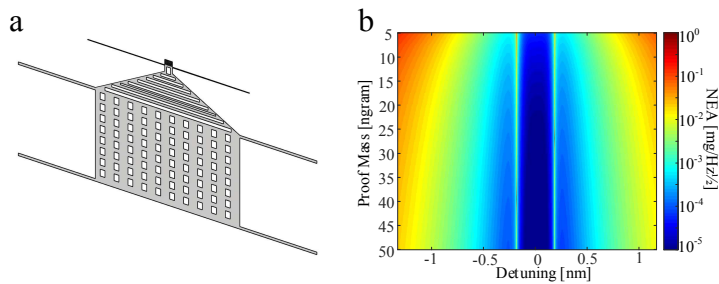


**Figure 13: Novel mass design.** a. Thinner beam is attached motional mass design. b. Thermal noise equivalent acceleration of the current design with respect to mass size.

Figure 13b shows thermal noise equivalent acceleration (NEA) for a fixed mechanical frequency; we achieve such behavior when we sweep the mass. As seen in the figure, thermal NEA decreases with increasing mass size.

Once we have the optimized design and fabricated device, we would like to test the new devices. We hope that the new design can reduce buckling, since it will increase the optical quality factor quite a lot, resulting in a higher mechanical quality factor and thus sensing resolution.

## 6 CONCLUSION

In conclusion, we introduced a new OMA nanofabrication technique that has the ability to avoid over-etching and high insertion loss and obtain low insertion loss as small as 24 dB. This value is already 4 times lower than the best insertion loss we achieved in our prior work (manuscript on the process). Additionally, we presented our measurement on the accelerometers, including optical measurements and mechanical domain measurements. However, finding a device with a decent optomechanical mode is not straightforward and requires tedious work after the fabrication process. We have to check each device for any potential buckling first. Unfortunately for us, more than 60 percent of the devices were buckled and there is a very slight chance that they could work. Therefore, it is crucial to resolve this problem. We introduced a novel mass design to circumvent the buckling. By adding 2 thin beams both sides of the photonic crystal will reduce the buckling on the crystal. The optical quality factor was reported as 4350 (8), and according to our simulations, quality factor should be at least  $\sim 3000$  to achieve meaningful optomechanical mode (this value is found for our existing device, we sweep the optical quality factor to see the mechanical quality factor). We hope that this new approach can achieve optical quality factor higher than it was reported before. Consequently, higher resolution than it was reported before (8) as  $8.2 \mu\text{g}/\text{Hz}^{1/2}$  could be achieved. Additionally, if the mass size is expanded by a couple orders of magnitude, this kind of devices can be used very delicate missions such as Grace without any need of high cost and size hybrid systems (24, 25, 26, 27).

## 7 REFERENCES

- [1] J. Kepler, 1619, *De cometis libelli tres* (Typis Andreae Aperiari).
- [2] T. J. Kippenberg, K. J. Vahala, Cavity optomechanics: Back-action at the mesoscale. *Science* **321**, 1172 (2008).
- [3] A. Krause, et. al., "A high-Resolution Microchip Optomechanical Accelerometer," *Nature Photonics* **6**, 11 (2012).
- [4] Y. Li, J. Zheng, et al. "Design of Dispersive Optomechanical Coupling and Cooling in Ultrahigh-Q/V slot-type Photonic Crystal Cavities." *Optics express* **18**, no. 23 (2010).
- [5] A. Schliesser, R. Riviere, G. Anetsberger, O. Arcizet, T.J. Kippenberg, Resolved-sideband cooling of a micromechanical oscillator. *Nature Phys.* **4**, 415–419 (2008)
- [6] M. Aspelmeyer, T. J. Kippenberg, and F. Marquardt, Cavity optomechanics, *Rev. Mod. Phys.* **86**(4), 1391 (2014)
- [7] A. Krause, et. al., "A high-Resolution Microchip Optomechanical Accelerometer," *Nature Photonics* **6**, 11 (2012).
- [8] Huang, Y., Flor, J. G., Li, Y., Wang, W., Wang, D., Goldberg, N., Zheng, J., Yu, M., Lu, M., Kutzer, M., Rogers, D., Kwong, D., Churchill, L., Wong, C. W., A Chip-Scale Oscillation-Mode Optomechanical Inertial Sensor Near the Thermodynamical Limits. *Laser & Photonics Reviews* **2020**, *14*, 1800329.

- [9] J. G. Flor Flores, W. Wang, Y. Huang, J. Wu, T. Yerebakan, Q. Bai, and C. W. Wong, Low-frequency noise stabilization in optomechanical inertial accelerometers for high-resolution sensing, *Proc. Conf. Lasers and Electro-Optics*, San Jose, CA (2020), paper SM4M.2.
- [10] Y. Huang, J. G. Flor Flores, Z. Cai, M. Yu, D.-L. Kwong, G. Wen, L. Churchill, and C. W. Wong, A low-frequency chip-scale optomechanical oscillator with 58 kHz mechanical stiffening and more than 100th-order stable harmonics, *Nature: Scientific Reports* **7**, 4383 (2017).
- [11] T. Weiss, A. Nunnenkamp, Quantum limit of laser cooling in dispersive and dissipative coupled optomechanical systems, *Physical Review*, **88** (2013).
- [12] X. Luan, Y. Huang, Y. Li, J. F. McMillan, J. Zheng, S.-W. Huang, P.-C. Hsieh, T. Gu, D. Wang, A. Hati, D. A. Howe, G. Wen, M. Yu, G. Lo, D.-L. Kwong, and C. W. Wong, An integrated low phase noise radiation-pressure-driven optomechanical oscillator chipset, *Nature: Scientific Reports* **4**, 6842 (2014).
- [13] J. Zheng, Y. Li, M. S. Aras, A. Stein, K. L. Shepard, and C. W. Wong, Parametric optomechanical oscillations in two-dimensional slot-type high- $Q$  photonic crystal cavities, *Appl. Phys. Lett.* **100**, 211908 (2012).
- [14] J. Gao, J. F. McMillan, M.-C. Wu, S. Assefa, and C. W. Wong, Demonstration of an air-slot mode-gap confined photonic crystal slab nanocavity with ultrasmall mode volumes, *Appl. Phys. Lett.* **96**, 051123 (2010).
- [15] Y.-C. Liu, Y.-F. Xiao, X. Luan, Q. Gong, and C. W. Wong, Coupled cavities for motional ground-state cooling and strong optomechanical coupling, *Phys. Rev. A* **91**, 033818 (2015).
- [16] J. Zheng, X. Sun, Y. Li, M. Poot, A. Dadgar, N. Shi, W. H. P. Pernice, H. X. Tang, and C. W. Wong, Femtogram dispersive L3-nanobeam optomechanical cavities: design and experimental comparison, *Optics Express* **20**, 26484 (2012).

- [17] Y. Huang, J. Wu, J. G. Flor Flores, M. Yu, D.-L. Kwong, G. Wen, and C. W. Wong, Synchronization in air-slot photonic crystal optomechanical oscillators, *Applied Physics Letters* **110**, 111107 (2017).
- [18] T. Yerebakan, J. G. Flor Flores, Y. Huang, W. Wang, J. Wu, and C. W. Wong, Thermodynamical bounds and noise of cavity optomechanical acceleration sensing. *Proc. Conf. Lasers and Electro-Optics*, San Jose, CA (2021)
- [19] J. G. Flor Flores, Y. Huang, T. Yerebakan, W. Wang, J. Wu, and C. W. Wong, Velocity random walk and dynamic range of laser-driven precision optomechanical inertial accelerometers. *Proc. Conf. Lasers and Electro-Optics*, San Jose, CA (2021)
- [20] JM. Courty, A. Heidmann, and M. Pinard, Quantum limits of cold damping with optomechanical coupling. *Eur. Phys. J. D* **17**, 399–408 (2001).  
<https://doi.org/10.1007/s100530170014>
- [21] K. Schneider and P. Seidler, Strong optomechanical coupling in a slotted photonic crystal nanobeam cavity with an ultrahigh quality factor-to-mode volume ratio, *Opt. Express* **24**, 13850-13865 (2016)
- [22] K. Schneider, Y. Baumgartner, S. Hönl, P. Welter, H. Hahn, D. J. Wilson, L. Czornomaz, and P. Seidler, "Optomechanics with one-dimensional gallium phosphide photonic crystal cavities," *Optica* **6**, 577-584 (2019)
- [23] M. L. Gorodetsky, A. Schliesser, G. Anetsberger, S. Deleglise, and T. J. Kippenberg, "Determination of the vacuum optomechanical coupling rate using frequency noise calibration," *Opt. Express* **18**, 23236-23246 (2010)

- [24] P. Abrykosov, R. Pail, T. Gruber, N. Zahzam, A. Bresson, E. Hardy, B. Christophe, Y. Bidel, O. Carraz, and C. Siemes, Impact of a novel hybrid accelerometer on satellite gravimetry performance, *Advances in Space Research*, **63** (2019)
- [25] R. Haagmans, C. Siemes, L. Massotti, O. Carraz, P. Silvestrin, ESA's next-generation gravity mission concepts, *Earth's Gravity and Earth Science*, **31**, (2020)
- [26] K. Bongs, R. Launay, M.A. Kasevich, High-order inertial phase shifts for time-domain atom interferometers, *Appl. Phys. B*, **84**, 599–602 (2006)
- [27] T. Kovachy, P. Asenbaum, C. Overstreet, *et al.* Quantum superposition at the half-metre scale. *Nature* **528**, 530–533 (2015).